ANL/NE-13/25

Verification and Validation of High-Fidelity Multi-Physics Simulation Codes for Advanced Nuclear Reactors (Year 2)

Nuclear Engineering Division

About Argonne National Laboratory
Argonne is a U.S. Department of Energy laboratory managed by UChicago Argonne, LLC under contract DE-AC02-06CH11357. The Laboratory's main facility is outside Chicago, at 9700 South Cass Avenue, Argonne, Illinois 60439. For information about Argonne and its pioneering science and technology programs, see www.anl.gov.

DOCUMENT AVAILABILITY

Online Access: U.S. Department of Energy (DOE) reports produced after 1991 and a growing number of pre-1991 documents are available free via DOE's **SciTech Connect** (http://www.osti.gov/scitech/)

Reports not in digital format may be purchased by the public from the National Technical Information Service (NTIS):

U.S. Department of Commerce
National Technical Information Service
5301 Shawnee Rd
Alexandra, VA 22312
www.ntis.gov
Phone: (800) 553-NTIS (6847) or (703) 605-6000
Fax: (703) 605-6900
Email: **orders@ntis.gov**

Reports not in digital format are available to DOE and DOE contractors from the Office of Scientific and Technical Information (OSTI):

U.S. Department of Energy
Office of Scientific and Technical Information
P.O. Box 62
Oak Ridge, TN 37831-0062
www.osti.gov
Phone: (865) 576-8401
Fax: (865) 576-5728
Email: **reports@osti.gov**

Disclaimer
This report was prepared as an account of work sponsored by an agency of the United States Government. Neither the United States Government nor any agency thereof, nor UChicago Argonne, LLC, nor any of their employees or officers, makes any warranty, express or implied, or assumes any legal liability or responsibility for the accuracy, completeness, or usefulness of any information, apparatus, product, or process disclosed, or represents that its use would not infringe privately owned rights. Reference herein to any specific commercial product, process, or service by trade name, trademark, manufacturer, or otherwise, does not necessarily constitute or imply its endorsement, recommendation, or favoring by the United States Government or any agency thereof. The views and opinions of document authors expressed herein do not necessarily state or reflect those of the United States Government or any agency thereof, Argonne National Laboratory, or UChicago Argonne, LLC.

ANL/NE-13/25

Verification and Validation of High-Fidelity Multi-Physics Simulation Codes for Advanced Nuclear Reactors (Year 2)

Prepared by
C. H. Lee and H. C. Lee*
Nuclear Engineering Division, Argonne National Laboratory

October 31, 2013

* The Korea Atomic Energy Research Institute

Project Number and Title: 2011-03-K, Verification and Validation of High-Fidelity Multi-Physics Simulation Codes for Advanced Nuclear Reactors

Lead U.S. Investigating Organization: Argonne National Laboratory (ANL)**,** 9700 South Cass Avenue**,** Argonne, Illinois USA

U.S. Principal Investigator: Changho Lee, ANL**,** Phone: +1-630-252-6086**,** Fax: +1-630-252-4978**,** E-mail: clee@anl.gov

Lead Collaborating Investigating Organization: Korea Atomic Energy Research Institute (KAERI), 989-111 Daedeok-daero, Yuseong-Gu, Daejeon, Korea

Lead Collaborating Principal Investigator: Hyun Chul Lee, KAERI**,** Phone: +82-42-868-4807**,** Fax: +82-42-868-8767**,** E-mail: lhc@kaeri.re.kr

Other Collaborating Organizations:

Reporting Period: 11/15/2012 – 10/15/2013

U.S. NTD/SIM: Keith S. Bradley

U.S. Work Package #: MS-12AN060311

Project Status Summary

The project objective is to verify and validate a suite of high-fidelity multi-physics simulation methods and codes developed during the previous I-NERI projects, against Monte Carlo solutions and experimental measurements for LWR and VHTR cores. Using benchmark problems developed during the previous year, ANL and KAERI continued to work on verifying the neutronics code DeCART and associated cross section libraries. Initial progress was also made on validating the code against experimental data. KAERI focused on verifying the DeCART code against numerical benchmark problems such as a PMR200 2-D pin cell/core and a HTTR 2-D block/core as well as improving DeCART capabilities such as the cross-section library group structure optimization, the fundamental and generalized adjoint equation solver, cylindrical boundary treatment, improved ray tracing, and implementing the direct resonance integral table method for resonance treatment. Verification test results for the updated capabilities showed substantial improvements in the estimation of eigenvalue and reaction rates.

Since the focus of the U.S./DOE NEAMS program supporting the I-NERI project was changed from LWR to SFR, the work scope of ANL had to be altered accordingly. Several sub-tasks in Task 2 and Task 3 were removed and instead a new task, Task 4 generation and verification of a generalized cross section library, was created with three sub-tasks. Consequently, this year ANL spent most of its effort on developing a generalized cross section library which can be applied to various reactor types including LWR, VHTR, and SFR. In addition, the development of the cross section application programming interface (API) was initiated to facilitate integration of the new cross section library into transport codes. Preliminary verification tests were performed for the generalized cross section library and API.

Project Organization:

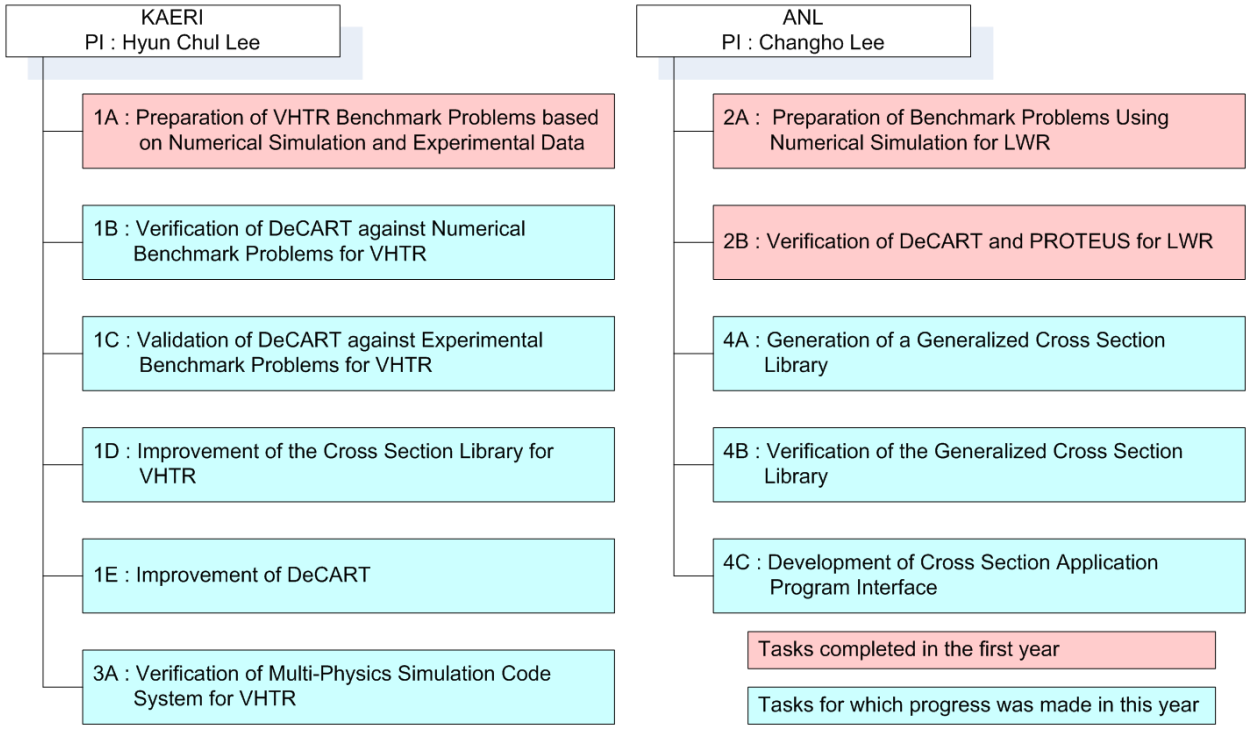

Narrative:

Task 1: Verification and Validation of Neutronics Code for VHTR (KAERI)

The goal of this task is to verify and validate the neutronics code DeCART for VHTR. Of 5 subtasks, 1A was completed last year and the remaining 4 tasks were performed this year which focus on updating and verifying DeCART capabilities and functions.

Task 1A: Preparation of VHTR Benchmark Problems based on Numerical Simulation and Experimental Data (KAERI)

This task was completed last year.

Task 1B: Verification of DeCART using Numerical Benchmark Problems for VHTR (KAERI)

The objective of this task is to verify the DeCART code using the numerical benchmark problems defined in Task 1A not only for single-effect tests but also for integral-effect tests. This year, more attention was paid to the integral-effect tests than the single-effect tests. To investigate the effect of the multi-group cross-section library, benchmark problems were generated for various VHTR pin-cell configurations. For integral-effect tests, benchmark calculations using the 2-D PMR200 depletion and 2-D HTTR [1] problems were performed by comparing the DeCART results with the reference McCARD results.

a) Multi-group Cross-section Library Test

In this sub-task, the accuracy of the DeCART 190-G cross-section library, based on ENDF/B-VII.0 data, was investigated by comparing the k_{inf} values of the DeCART code with those of the McCARD code for various VHTR pin-cell configurations. Table 1 shows 31 VHTR pin-cell configurations with different enrichments, packing fractions, presence of burnable poisons (BPs) in the fuel block, and temperatures. Table 1 also shows the reference k_{inf} values for the cases obtained from the McCARD code with the ENDF/B-VII.0 cross-section library. Figure 1 shows the DeCART errors for the cases with the DeCART library or the HELIOS-1.9 library. With the DeCART library, k_{inf} values are underestimated in the zero-burnup cases up to about -750pcm, while they are overestimated in the burnt cases up to about +250 pcm. With the HELIOS library, k_{inf} values are overestimated in most cases and the maximum error is about +550pcm. There would be two possible sources for the relatively large errors. One is the multi-group cross-sections themselves generated by NJOY with a neutron spectrum defined by combining the Maxwellian distribution for the thermal range, the 1/E distribution for the intermediate range, and the fission spectrum for the fast range. The other is the resonance integral tables generated by the MERIT code, especially for U-238. The effects of the two sources will be investigated closely and the DeCART cross-section library will be improved by removing the errors from the multi-group cross-sections and the resonance integral tables.

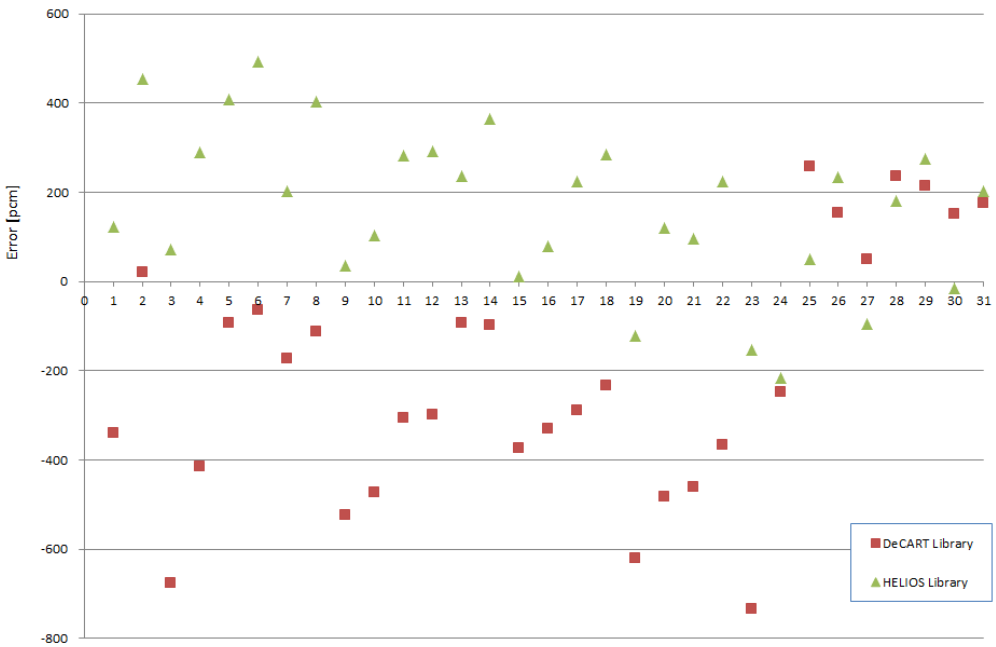

Figure 1. DeCART Errors for the Cases with DeCART Library and HELIOS Library

Table 1. Specifications and McCARD Reference Solutions for the 31 Cases

Case #	Case ID	Burnup [GWD/TU]	Enrich. [%]	Packing Fraction [%]	BP in Block	Temp. [K]	McCARD	
							k_{inf}	S.D. [pcm]
1	F05P10No10	Fresh	5.0	10	No	1000	1.47469	12
2	F05P10B10	Fresh	5.0	10	Boron	1000	0.52314	9
3	F05P30No10	Fresh	5.0	30	No	1000	1.26402	15
4	F05P30B10	Fresh	5.0	30	Boron	1000	0.78033	15
5	F05P50No10	Fresh	5.0	50	No	1000	1.11907	17
6	F05P50B10	Fresh	5.0	50	Boron	1000	0.82091	16
7	F20P10No10	Fresh	20.0	10	No	1000	1.67107	15
8	F20P10B10	Fresh	20.0	10	Boron	1000	1.09600	17
9	F20P30No10	Fresh	20.0	30	No	1000	1.40071	18
10	F20P30B10	Fresh	20.0	30	Boron	1000	1.20490	18
11	F20P50No10	Fresh	20.0	50	No	1000	1.27031	16
12	F20P50B10	Fresh	20.0	50	Boron	1000	1.16843	16
13	F30P10No10	Fresh	30.0	10	No	1000	1.69747	15
14	F30P10B10	Fresh	30.0	10	Boron	1000	1.25110	18
15	F30P30No10	Fresh	30.0	30	No	1000	1.43334	16
16	F30P30B10	Fresh	30.0	30	Boron	1000	1.29631	16
17	F30P50No10	Fresh	30.0	50	No	1000	1.32362	16
18	F30P50B10	Fresh	30.0	50	Boron	1000	1.25556	16
19	F20P30No03	Fresh	20.0	30	No	300	1.48757	16
20	F20P30B03	Fresh	20.0	30	Boron	300	1.27558	17
21	F20P30No12	Fresh	20.0	30	No	1200	1.38427	16
22	F20P30B12	Fresh	20.0	30	Boron	1200	1.19032	18
23	B05P10No10	100	5.0	10	No	1000	0.76243	11
24	B05P30No10	100	5.0	30	No	1000	0.70312	14
25	B05P50No10	100	5.0	50	No	1000	0.57491	14
26	B20P10No10	100	20.0	10	No	1000	1.32145	15
27	B20P30No10	100	20.0	30	No	1000	0.99838	15
28	B20P50No10	100	20.0	50	No	1000	0.86710	14
29	B30P10No10	100	30.0	10	No	1000	1.42472	15
30	B30P30No10	100	30.0	30	No	1000	1.10805	14
31	B30P50No10	100	30.0	50	No	1000	0.99978	14

∗ S. D. : standard deviation

b) Verification of DeCART using PMR200 Numerical Benchmark

In this sub-task, the full core depletion functionality of DeCART was verified using a 2-D PMR200 numerical benchmark shown in Fig. 2(a). Figure 2(b) shows the DeCART 1/12 core model for PMR200. Depletion calculations for the core without or with burnable poison (BP) were carried out using the DeCART code and the results were compared with the reference solutions obtained from the McCARD code. Note that the 190-G cross-section library was used in the DeCART calculation.

Figure 3 compares the multiplication factors of the two codes for the two cases. In the case without BP, DeCART code underestimates the multiplication factor by about 400pcm during the whole depletion period, which is consistent with the results for the pin cell cases described in the previous sub-task. In the case with BP, in contrast, a large positive error is introduced in the middle of the depletion calculation and the error goes up to +350pcm at the middle of cycle (MOC). In the next year, the cause of the large positive error observed in the middle of the depletion calculation will be investigated more closely.

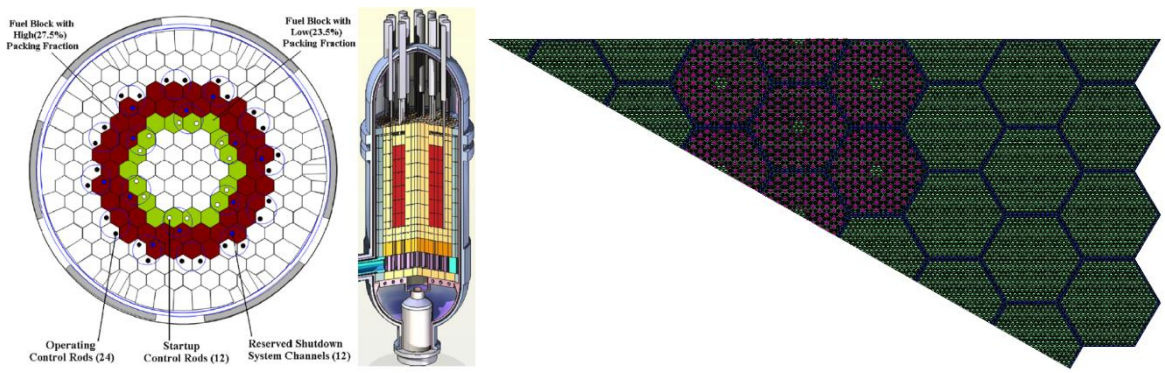

(a) PMR 200 Reactor (b) 1/12 Core Model of PMR200

Figure 2. PMR200 Reactor and 1/12 Core Model

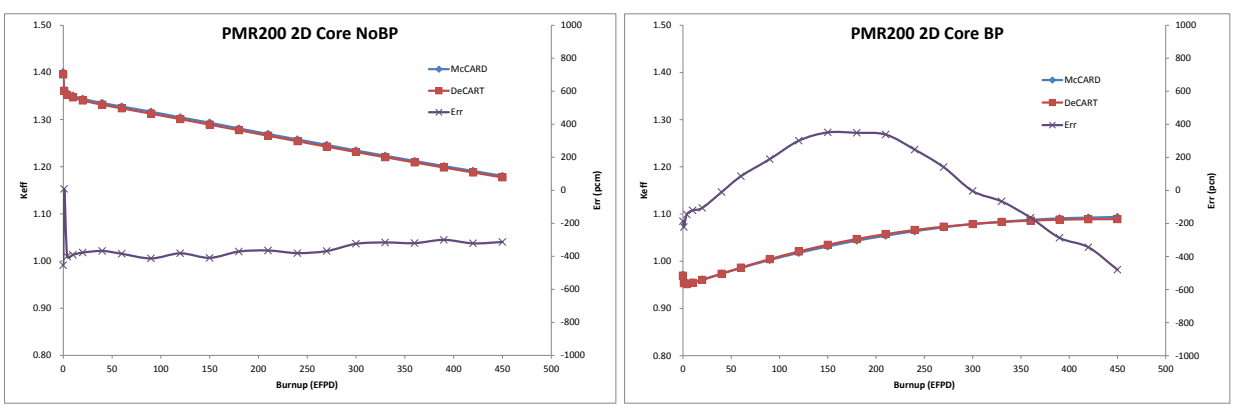

(a) Core without BP (b) Core with BP

Figure 3. Effective Multiplication Factor for PMR200 Core

c) Verification of DeCART using HTTR Numerical Benchmark

In this sub-task, the cell, block, and full core depletion functionality of DeCART was verified using a HTTR numerical benchmark shown in Figure 4. The 190-G cross-section library was used in this DeCART calculation, and the double heterogeneity of a fuel pin was treated in the code. Table 2 shows the temperature variation results for the single cell and single block models shown in Fig. 4(a) and Fig 4(b), respectively. The effective multiplication factors from DeCART agreed within 80 pcm with the McCARD solutions.

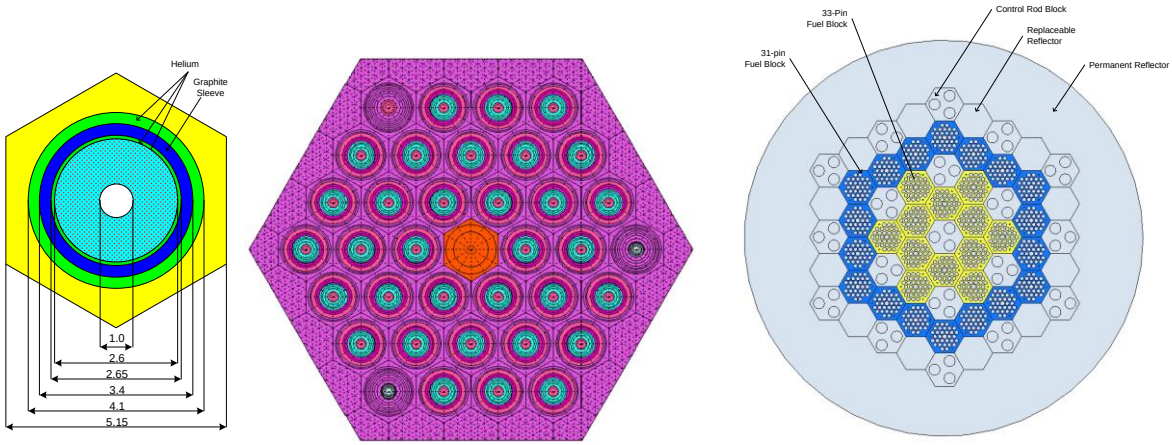

(a) Pin Model (b) Block Model (c) Core Model

Figure 4. Pin, Block, and Core Model of HTTR

Table 2. Results for Temperature Variation Calculations

T_m [K]	T_f [K]	Single Cell Model			Single Block Model		
		McCARD	DeCART		McCARD	DeCART	
		k_{inf}(M)	k_{inf}(D)	$\Delta\rho$ (D-M) [pcm]	k_{inf}(M)	k_{inf}(D)	$\Delta\rho$ (D-M) [pcm]
700	700	1.28376	1.28395	11.5	1.17919	1.17860	-42.5
700	800	1.27363	1.27330	-20.3	1.17344	1.17248	-69.8
700	900	1.26356	1.26341	-9.4	1.16785	1.16679	-77.8
800	800	1.27119	1.27156	22.9	1.16698	1.16641	-41.9
800	900	1.26158	1.26169	6.9	1.16143	1.16075	-50.4
800	1000	1.25241	1.25246	3.2	1.15614	1.15545	-51.7
1000	1000	1.24982	1.24956	-16.6	1.14560	1.14484	-57.9
1000	1100	1.24155	1.24091	-41.5	1.14072	1.13990	-63.1
1000	1200	1.23385	1.23267	-77.6	1.13590	1.13516	-57.4
1200	1200	1.23025	1.23041	10.6	1.12606	1.12593	-10.3
1200	1300	1.22278	1.22258	-13.4	1.12177	1.12146	-24.6
1200	1400	1.21546	1.21510	-24.4	1.11761	1.11717	-35.2
1200	1500	1.20838	1.20793	-30.8	1.11344	1.11306	-30.7

Figure 5(a) shows the DeCART 2-D 1/6 core model for the HTTR. The new functionality of the DeCART code for cylindrical boundaries described in Task 1E(c) was utilized in this calculation. Table 3 shows the results for the temperature variation calculations. The k_{eff} errors were about 500pcm, which were relatively large compared to the single cell and single block

cases but they are still acceptable. Figure 5(b) shows the depletion calculation results for the HTTR 2-D 1/6 core model shown in Fig. 5(a). The maximum k_{eff} error, about 500 pcm, occurs at the fresh core state.

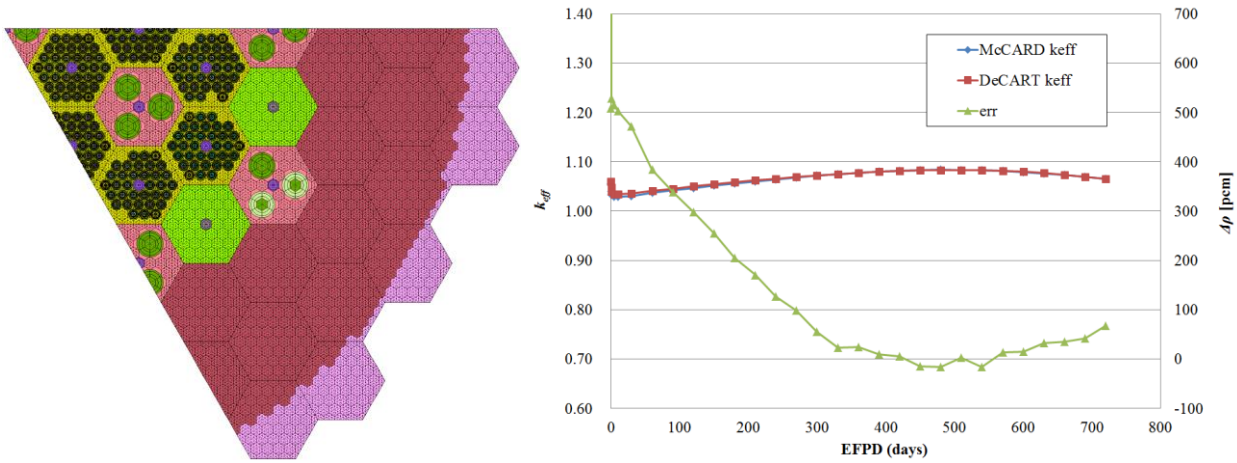

(a) DeCART 2-D 1/6 Model for HTTR (b) Depletion Calculation Results

Figure 5. DeCART 2-D Model and Depletion Calculation Results for HTTR

Table 3. Temperature Variation Results for 2-D Core

T_m [K]	T_f [K]	McCARD	DeCART		McCARD	DeCART		McCARD	DeCART	
		k_{eff}(M)	k_{eff}(D)	$\Delta\rho$ (D-M) [pcm]	k_{eff}(M)	k_{eff}(D)	$\Delta\rho$ (D-M) [pcm]	k_{eff}(M)	k_{eff}(D)	$\Delta\rho$ (D-M) [pcm]
		T_i=700K, T_o=700K			T_i=1000K, T_o=1000K			T_i=1000K, T_o=700K		
700	700	1.08324	1.08865	458.8	-	-	-	-	-	-
700	900	1.07599	1.08128	454.7	-	-	-	-	-	-
800	900	1.06743	1.07311	495.9	-	-	-	-	-	-
1000	1000	1.04927	1.05505	522.1	1.05460	1.06028	508.0	1.05174	1.05724	494.6
1000	1200	1.04334	1.04906	522.6	1.04885	1.05428	491.1	1.04576	1.05125	499.4
1200	1200	1.02988	1.03589	563.3	1.03545	1.04139	550.9	1.03233	1.03834	560.7
1200	1300	1.02729	1.03313	550.3	1.03285	1.03863	538.8	1.02978	1.03557	542.9
1200	1500	1.02217	1.02795	550.1	1.02788	1.03344	523.4	1.02481	1.03039	528.4

Task 1C: Validation of DeCART against Experimental Benchmark Problems for VHTR (KAERI)

The purpose of this task is to validate the DeCART code against the physics experiment of the HTTR [1]. In this year, the 3-D McCARD core model was established for a reference calculation. Figure 6 compares the McCARD results with those of the experiments. The first criticality was achieved with 17 and 18 fuel columns when the ENDF/B-VII.0 library and ENDF/B-VII.1 library was used, respectively, while the first criticality was achieved with 19 columns in the experiment. The McCARD code overestimates the multiplication factors by 1500pcm-3000pcm with the ENDF/B-VII.0 library and by 500pcm-1500pcm with the ENDF/B-VII.1 library.

Recently, new data for the HTTR start-up core such as air in graphite, impurities in dummy fuel blocks, and temporary neutron detector for start-up have been provided [2], which may affect the multiplication factor. In the next year, the 3-D DeCART model will be developed and the McCARD model will be modified in accordance with the new data provided. The calculation results will be compared with the experimental data.

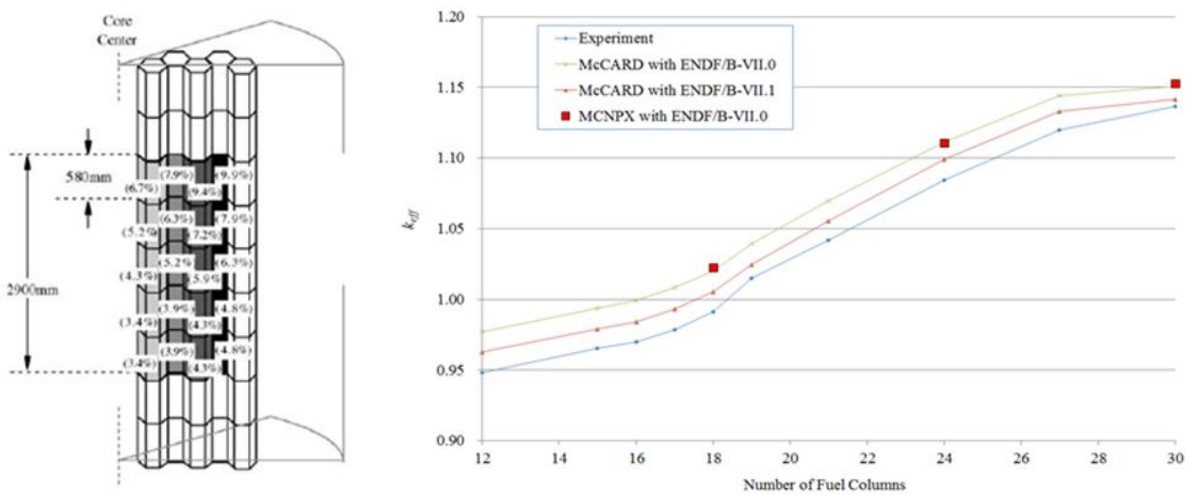

(a) 3-D core configuration (b) McCARD Reference Results for the Start-up Test

Figure 6. HTTR Core Configuration and the McCARD Reference Results for the Start-up Test

Task 1D: Improvement of the Cross-Section Library for VHTR (KAERI)

The objective of this task is to improve the DeCART cross-section library generated for VHTR as part of the previous I-NERI project. In this year, we developed a methodology for optimizing the neutron group structure of the cross-section library similar to that described in reference 3 for optimization of few-group structure in nodal codes. Figure 7 shows the basic idea of the group structure optimization. Suppose that we have fine group real flux and cross-sections for a system and we also have an approximate fine group spectrum slightly different from the real spectrum, for example, a spectrum defined by combining the Maxwellian distribution for the thermal range, *1/E* distribution for the intermediate range, and the fission spectrum for the fast range. If we introduce a coarse group structure, we can calculate the coarse group real flux and the coarse group cross sections by condensing the fine group cross-sections with the fine group approximate spectrum as a weighting function. Once we get the coarse group cross-sections and coarse group real flux, we can get approximate coarse group reaction rates by multiplying them. On the other hand, we can obtain the coarse group real reaction rate from the fine group cross-sections and fine group real flux. The errors of the approximate coarse group reaction rates depend on the approximate fine group spectrum and the coarse group structure. We can control the error of the approximate coarse group reaction rates by adjusting the coarse group structure with a given approximate fine group spectrum.

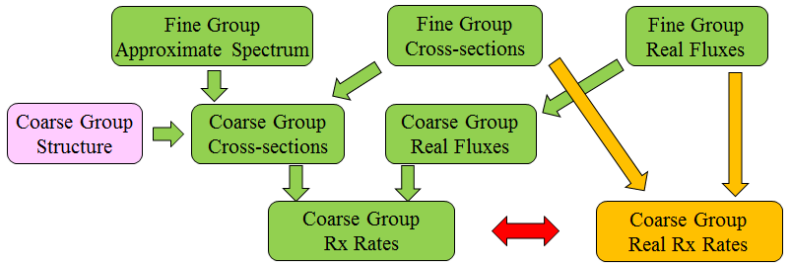

Figure 7. Group structure Optimization of the Cross-section Library

The following shows the algorithm of the group optimization procedure developed.

(1) Tally fine group fluxes ϕ_g^i and macroscopic cross-sections Σ_{xg}^i from Monte-Carlo calculations for N different pin cell configurations. $\left(g=1,2,\cdots,M;\, i=1,2,\cdots,N\right)$

(2) Choose an approximate fine group spectrum φ_g.

(3) Set $G=1$ and $g=1$.

(4) Include g^{th} fine group in the Gth coarse group.

(5) Calculate the actual G^{th} coarse group reaction rates R_{xG}^i with the fine group fluxes and cross-sections for the N pin-cell configurations. $\left(R_{xG}^i=\sum_{g'\in G}\Sigma_{xg'}^i\phi_{g'}^i;\, i=1,2,\cdots,N\right)$

(6) Calculate the actual G^{th} coarse group fluxes Φ_G^i with the fine group fluxes for the N pin cell configurations. $\left(\Phi_G^i=\sum_{g'\in G}\phi_{g'}^i;\, i=1,2,\cdots,N\right)$

(7) Calculate the approximate G^{th} coarse group cross-sections $\overline{\Sigma}_{xG}^i$ with the approximate spectrum for the N pin-cell configurations. $\left(\overline{\Sigma}_{xG}^i=\sum_{g'\in G}\Sigma_{xg'}^i\varphi_{g'}\Big/\sum_{g'\in G}\varphi_{g'};\, i=1,2,\cdots,N\right)$

(8) Calculate the approximate G^{th} coarse group reaction rates $\overline{R}_{xG}^i$ with the Gth coarse group fluxes Φ_G^i and the approximate G^{th} coarse group cross-sections $\overline{\Sigma}_{xG}^i$. $\left(\overline{R}_{xG}^i=\overline{\Sigma}_{xG}^i\Phi_G^i;\, i=1,2,\cdots,N\right)$

(9) Calculate the errors. $\left(\varepsilon_{xG}^i=\left(\overline{R}_{xG}^i-R_{xG}^i\right)\Big/\sum_{g'=1}^{M}\Sigma_{xg'}^i\phi_g^i;\, i=1,2,\cdots,N\right)$

(10) If all the errors are less than a specified criterion, set $g\leftarrow g+1$ and go to step (4). Otherwise, set $G\leftarrow G+1$, $g\leftarrow g+1$ and go to step (4).

(11) Repeat until $g=M$.

A program for group structure optimization was developed and used for a preliminary group optimization calculation. First, fine group (950-G) macroscopic absorption cross-sections and nu-fission ($\nu\Sigma_f$) cross-sections were tallied for 8 VHTR pin cell configurations by using the McCARD Monte Carlo code. Table 4 shows the VHTR pin cell configurations. The fine group flux of Case 1 was selected as the approximate fine group spectrum to be used in the group collapsing.

Table 4. VHTR Pin Cell Configurations for Group Structure Optimization

Case	Fuel	Enrichment (%)	Packing Fraction (%)	Burnable Poison
1	Fresh UO_2	5	10	0
2	Fresh UO_2	5	10	BP
3	Fresh UO_2	5	50	0
4	Fresh UO_2	5	50	BP
5	Fresh UO_2	30	10	0
6	Fresh UO_2	30	10	BP
7	Fresh UO_2	30	50	0
8	Fresh UO_2	30	50	BP

Table 5 shows the results of the preliminary group optimization calculation. The optimized group structure has fewer fast groups, more resonance groups, and similar number of thermal groups in comparison with the HELIOS 190-G structure which is adopted in the DeCART 190-G cross-section library. Figure 8 shows the group-wise macroscopic cross-sections and the reaction rate errors in the resonance energy range for the conventional 190-G and new group structure. From Fig. 8, more energy groups are placed in the resonance peaks while less energy groups are placed in the valleys between the peaks. In the next year, the group structure optimization will be conducted for the DeCART multi-group cross-section library for VHTR using the group structure optimization procedure developed this year.

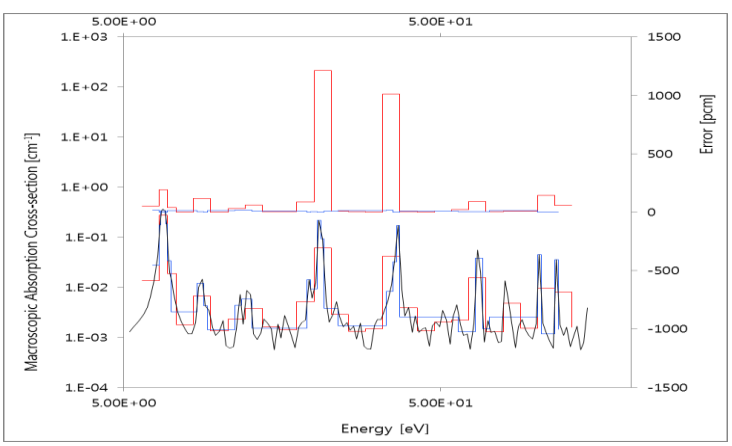

Figure 8. Group-wise Macroscopic Cross-sections and Reaction Rate Errors

Table 5. Results of the Preliminary Group Optimization Calculation

Criterion [pcm]	1	5	10	20	HELIOS 190-G
# of Fast Groups	16	8	7	5	63
# of Resonance Groups	130	72	51	40	69
# of Thermal Groups	69	38	27	20	58
Total # of Groups	215	118	85	65	190

Task 1E: Improvement of DeCART (KAERI)

The objective of this task is to implement new functions for practical core calculations and to improve the existing modules for user convenience or computational efficiency. Several new functions were implemented into the DeCART code this year. Fundamental and generalized adjoint flux solvers were implemented for sensitivity and uncertainty analysis. A new boundary treatment model was developed to treat a cylindrical boundary. The Gaussian azimuthal angle discretization developed last year was implemented. The direct RIT (Resonance Integral Table) method for resonance treatment was implemented to remove the difficulties in generating the subgroup data.

a) Implementation of the Fundamental Mode Adjoint Flux Solver

Two solution methods for the fundamental mode adjoint flux were implemented in the DeCART code. One is to solve the adjoint neutron transport equation directly, and the other is to solve the adjoint B1 criticality equation. The block-wise adjoint B1 criticality equation with the homogenized block cross-sections is solved whenever the forward criticality calculation is performed because the additional computational burden is trivial and DeCART prints out the assembly averaged adjoint flux. The adjoint neutron transport calculation is performed when requested by the user, whose computational burden is similar to the forward transport calculation. For efficiently solving the adjoint neutron transport equation, the CMFD acceleration was adopted as it was in solving the forward neutron transport equation.

The adjoint transport equation can be written as:

$$-\Omega \cdot \nabla \varphi_g^*(\mathbf{r},\mathbf{\Omega}) + \Sigma_g \varphi_g^*(\mathbf{r},\mathbf{\Omega}) = q_g^*(\mathbf{\Omega}), \tag{1}$$

where

$$q_g^*(\mathbf{\Omega}) = \frac{1}{4\pi}\left[\frac{\nu\Sigma_{f\,g}}{k}\sum_{g'}\chi_{g'}(\mathbf{r})\phi_{g'}^* + \sum_{g'}\Sigma_{\mathbf{s}\,g\to g'}\phi_{g'}^*\right].$$

For the flat source region, the MOC solution of adjoint flux can be derived as:

$$\varphi_g^*(0,\mathbf{\Omega}_\mathbf{r}) = \varphi_g^*(R,\mathbf{\Omega}_\mathbf{r})\exp\left(-\frac{\Sigma s}{\sin\theta}\right) + \frac{q_g^*(\mathbf{\Omega}_\mathbf{r})}{\Sigma}\left[1-\exp\left(-\frac{\Sigma s}{\sin\theta}\right)\right]. \tag{2}$$

The difference between the final expressions of the adjoint and the forward solutions is the boundary condition in a ray segment. The incoming adjoint angular flux can be obtained using

the above adjoint equation for a given outgoing adjoint angular flux while the outgoing forward angular flux can be obtained using the forward equation for a given incoming forward angular flux. Therefore, the adjoint angular flux is obtained through the back tracing.

The adjoint B1 criticality equation can be written as:

$$\Sigma_g \psi_g^* - \sum_h \Sigma_{0,g\to h} \psi_h^* \pm iBJ_g^* = \nu\Sigma_{fg}, \tag{3a}$$

$$3\alpha_g(B)\Sigma_g J_g^* - 3\sum_h \Sigma_{1,g\to h} J_h^* = \mp iB\psi_g^*. \tag{3b}$$

The final expression for the adjoint critical spectrum can be derived as:

$$\mathbf{A}^* \vec{\psi}^* = \vec{F}^*. \tag{4}$$

The governing matrix $\mathbf{A}^*$ is the transpose matrix of $\mathbf{A}$ which is the governing matrix for the forward critical spectrum. Therefore, DeCART produces the assembly averaged critical adjoint flux by using the transpose matrix of $\mathbf{A}$. The infinite adjoint flux is also simply generated by setting the buckling (B) to zero.

The fundamental mode adjoint flux solver newly implemented in the DeCART code was verified using the PMR200 single block problem. Figure 9(a) compares the assembly averaged adjoint fluxes obtained from the adjoint transport equation and the B1 criticality equation. The two solutions agree well with each other showing less than 1.0% error. Figure 9 compares the local adjoint fluxes at the moderator, inner fuel, and outer fuel regions obtained by solving the adjoint transport equation.

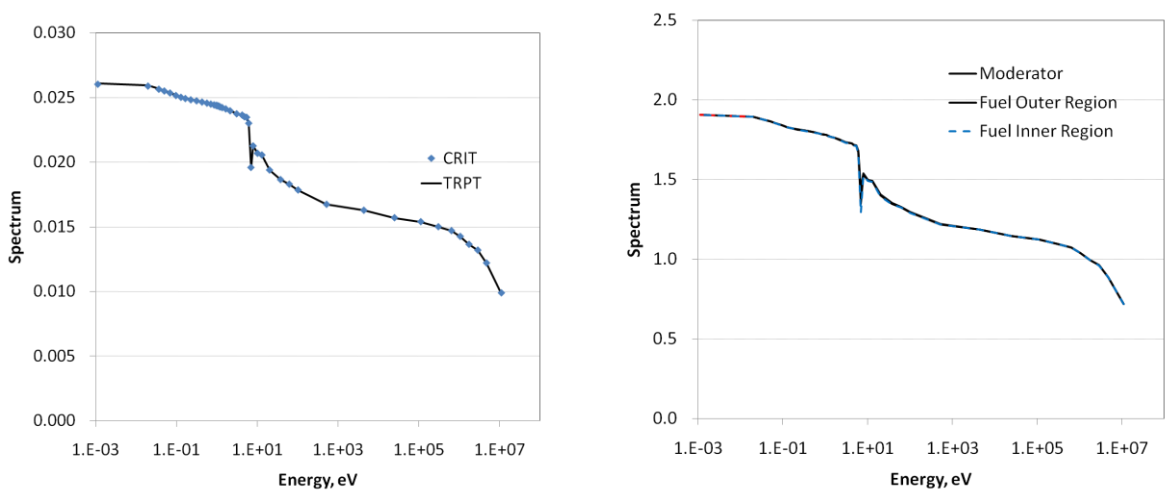

(a) Two Adjoint Fluxes (b) Local Adjoint Fluxes

CRIT: Adjoint flux from adjoint B1 Criticality Calculation

TRPT: Adjoint flux from adjoint transport calculation

Figure 9. Comparison of the Adjoint Fluxes for PMR200 Block

b) Implementation of the Generalized Adjoint Flux Solver

The generalized adjoint flux solver based on the generalized perturbation theory was implemented in the DeCART code for the sensitivity and uncertainty analysis of general responses such as cross sections and the power density. The general response is expressed as the following equation:

$$R = \frac{\langle H_1(\alpha), \phi(\alpha) \rangle}{\langle H_2(\alpha), \phi(\alpha) \rangle}. \tag{5}$$

A small perturbation of the general response can be approximated as the following equation:

$$\frac{\delta R}{R} \cong \left\langle \left(\frac{\delta H_1}{\langle H_1, \phi \rangle} - \frac{\delta H_2}{\langle H_2, \phi \rangle} \right), \phi \right\rangle + \left\langle \left(\frac{H_1}{\langle H_1, \phi \rangle} - \frac{H_2}{\langle H_2, \phi \rangle} \right), \delta\phi \right\rangle. \tag{6}$$

The first term of the right side of Eq. (6) is the direct component which can be calculated easily from its definition, and the second term of the right side of Eq. (6) is the indirect component which includes the solution of the perturbed system and cannot be simply calculated. If we solve the following generalized adjoint equation:

$$(A^* - \lambda B^*)\Gamma^* = S^* \equiv \frac{H_1}{\langle H_1, \phi \rangle} - \frac{H_2}{\langle H_2, \phi \rangle}, \tag{7}$$

with a constraint

$$\langle \Gamma^*, B\phi \rangle = 0. \tag{8}$$

Eq. (6) can be expressed as follows :

$$\frac{\delta R}{R} \cong \left\langle \left(\frac{\delta H_1}{\langle H_1, \phi \rangle} - \frac{\delta H_2}{\langle H_2, \phi \rangle} \right), \phi \right\rangle + \langle \Gamma^* (\delta A - \lambda \delta B), \delta\phi \rangle. \tag{9}$$

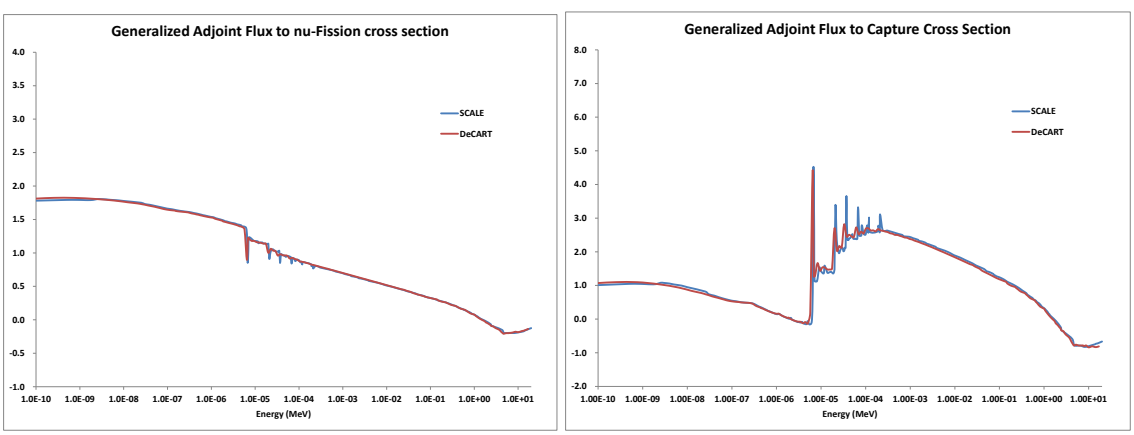

(a) U-235 nu-Fission Cross-section (b) U-238 Capture Cross-section

Figure 10. Generalized Adjoint Flux for the Cross Section Responses

A module for solving the generalized adjoint equation, Eq. (9), was implemented in the DeCART code. Figure 10 compares of the generalized adjoint fluxes for the nu-fission and capture cross section of U-235 by the DeCART code and those by the SCALE code. The two results are in good agreement except in the resonance energy ranges. The differences in the resonance energy range are attributed to the discrepancies in the resonance treatment between the two codes.

c) Cylindrical Boundary Treatment

An approximate model for the vacuum boundary condition on the cylindrical boundary was implemented in the DeCART code. The vacuum boundary condition can be replaced with the black absorber model which is defined by filling the outside of the boundary with a black absorber. For s convex boundary, the black absorber model essentially gives the same results as those in the model with vacuum boundary conditions. In contrast, the replacement of vacuum boundary condition with the black absorber model for a concave boundary as shown in 11(b) has some effect on the calculation results because the black absorber model does not allow the re-entrance of neutrons unlike the vacuum boundary condition model shown in Fig. 11(a). However, this effect is trivial on the calculation results as shown in Table 6 because the flux is very low on the boundary.

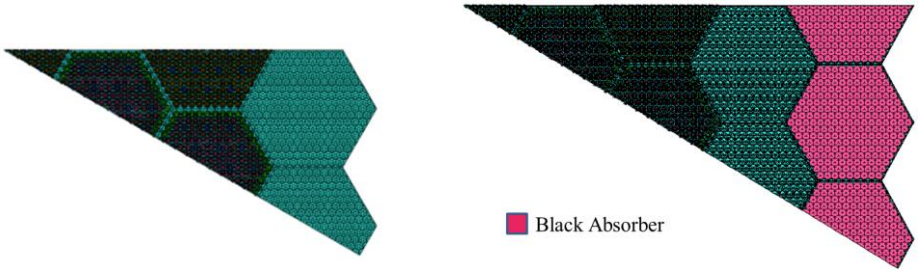

(a) Vacuum Boundary Model (b) Black Absorber Model

Figure 11 Replacement of Vacuum Boundary Condition with a Black Absorber Model

Table 6. Results for the Vacuum Boundary Model and the Black Absorber Model

Model	k_{eff}	Normalized Power Density			
		Block 1	Block 2	Block 3	Block 4
Vacuum BC	1.162220	1.9956	0.9199	1.3359	0.5782
Black Absorber	1.162220	1.9956	0.9199	1.3359	0.5782

To treat the cylindrical boundary, the BARREL card was added to the GEOM block of the DeCART input. In this card, a user can define not only the barrel configuration such as the barrel inner/outer radius, and barrel material but also the material for the barrel outer region. The DeCART code fills the cells with the barrel material or barrel outer material depending on the position of the cell centers. The implemented model was examined for the C5G7 hexagonal variation problem with a cylindrical boundary. Figure 12 shows the exact model and the approximate model using the BARREL card. Table 7 compares the results of the two models.

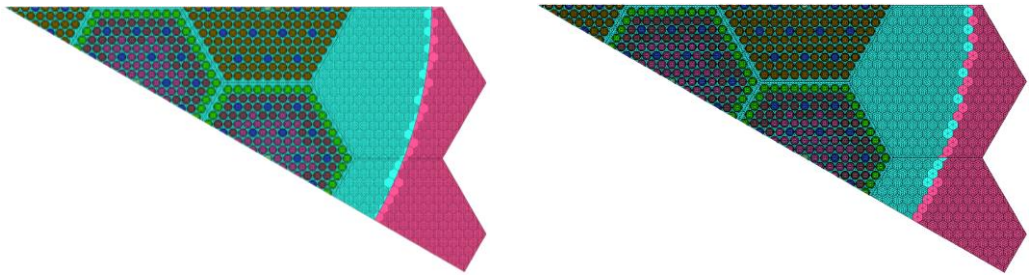

(a) Explicit Cylindrical Boundary Model (b) Approximate Cylindrical Boundary Model

Figure 12. Exact and Approximate Cylindrical Boundary Models

Table 7. Results for the Vacuum Boundary Model and the Black Absorber Model

Model	k_{eff}	Normalized Power Density			
		Block 1	Block 2	Block 3	Block 4
Exact Cylinder	1.162077	1.9992	0.9200	1.3377	0.5757
Approximate Cylinder	1.162072	1.9994	0.9200	1.3378	0.5756
Difference	-0.5pcm	+0.01%	0.00%	+0.01%	-0.02%

d) Azimuthal Angle Treatment based on Gaussian Quadrature

The azimuthal angle discretization method based on the Gaussian Quadrature was studied last year [4] but it was not implemented in the DeCART code due to the violation of the modular ray conditions. This year, the Gaussian azimuthal angle discretization was implemented in the DeCART code by adjusting the generated angle to meet the modular ray conditions. Then, the quadrature weights generated using the following equation as in the Gauss integration were adopted:

$$\begin{bmatrix} P_0(x_1) & P_0(x_2) & \cdots & P_0(x_n) \\ P_1(x_1) & P_1(x_2) & \cdots & P_1(x_n) \\ \cdots & \cdots & \cdots & \cdots \\ P_{n-1}(x_1) & P_{n-1}(x_2) & \cdots & P_{n-1}(x_n) \end{bmatrix} \begin{bmatrix} w_1 \\ w_2 \\ \cdots \\ w_n \end{bmatrix} = \begin{bmatrix} 2 \\ 0 \\ \cdots \\ 0 \end{bmatrix} \tag{10}$$

The conventional angle domain weight which uses the following equation was also examined.

$$w_k = \frac{1}{2\pi}\left[\frac{1}{2}(\varphi_k + \varphi_{k+1}) - \frac{1}{2}(\varphi_{k-1} + \varphi_k)\right] \tag{11}$$

The new azimuthal angle discretization methods were tested using the PMR200 single block problem. In this problem, three types of azimuthal angle discretization method were examined: the conventional method with angle domain weights (M0), the Gaussian angle with the quadrature weights (M1), and the Gaussian angle with angle domain weights (M2). Figure 13 shows the computational results with the three options. The performance of the M0 option was the worst showing about 200 pcm error with the default ray options. The M2 option showed the best performance of about 20 pcm error with the default ray options, as well as a very fast

convergence with the finer ray options. Therefore, M2 was adopted as a default method for the azimuthal angle discretization in the DeCART code.

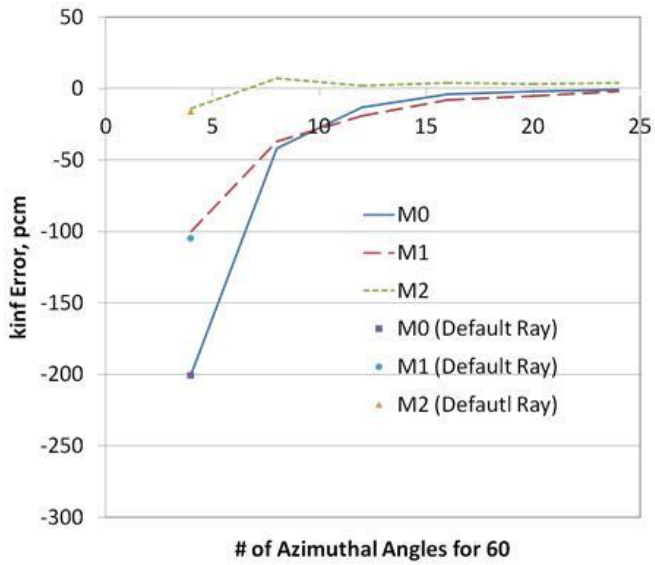

Figure 13. Eigenvalue Error Comparisons to the Azimuthal Angle Discretization Methods

e) RIT Method for Resonance Treatment

The direct resonance integral table (RIT) method [5] for the resonance treatment was developed to remove the difficulties in subgroup data generation and implemented into the DeCART code and examined for various rectangular problems by comparing with the KARMA [6] results. In the DeCART library, the resonance integral is tabulated as a function of background cross section and temperature. The direct RIT method uses RIT directly instead of the subgroup data to generate the resonance cross section.

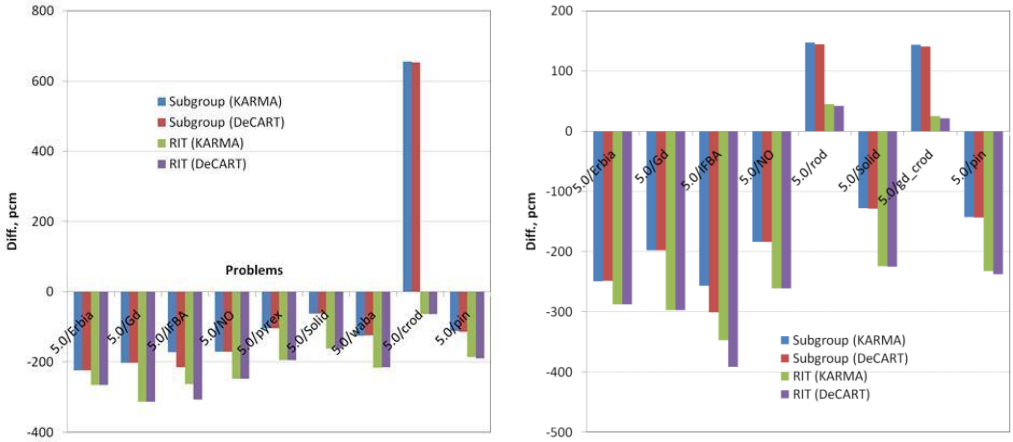

(a) 17x17 Assembly (b) 16x16 Assembly

Figure 14. Eigenvalue Error Comparisons for PWR Fuel Assembly Problems

The RIT method implemented in the DeCART code was examined for the 17x17 and 16x16 rectangular PWR assembly problems with various burnable poisons, and the results were compared with KARMA which uses the same solution method for the transport equation. Figure 14 shows the eigenvalue errors of the KARMA and DeCART codes compared to MCNP results for the various 17x17 and 16x16 problems. The two codes with both the subgroup and RIT methods produced very similar errors which indicate that the RIT method was correctly implemented in the DeCART code.

Task 2: Verification and Validation of Neutronics Code for LWR (Argonne)

The goal of this task is to verify and validate the neutronics codes DeCART and possibly PROTEUS for LWRs. This task was composed of six sub-tasks among which the verification of DeCART for LWR was performed in the first year. Since the focus of the NEAMS program supporting the I-NERI project was changed from LWR to SFR in FY13, the work scope of ANL had to be altered accordingly. Therefore, the work scope of Task 2 was reduced to contain only the two sub-tasks. A sub-task of Task 3 related to LWR was removed as well. Instead, a new task, Task 4, was created to focus on the generation and verification of cross section libraries for various reactor types including LWR, VHTR, and SFR.

Task 2A: Preparation of Benchmark Problems Using Numerical Simulation for LWR (Argonne)

This task was completed last year.

Task 2B: Verification of DeCART for LWR (Argonne)

This task was completed last year.

Task 3: Verification of Multi-physics Simulation Code System for VHTR (KAERI)

The goal of this task is to develop numerical benchmark problems for verification and to collect and build experimental data for validation of the multi-physics simulation code systems of KAERI and Argonne.

Task 3A: Verification of Multi-Physics Simulation Code System for VHTR (KAERI)

According to the strategy of KAERI, the DeCART code is coupled with the CORONA code for thermo-fluid information in a VHTR core. In the last I-NERI project, verification studies of the coupled analysis of DeCART/CORONA were made using simple conceptual benchmark problems (i.e., single fuel column and seven fuel column problems). In the present I-NERI project, the benchmark is extended to a whole core problem. In other words, a full core coupled analysis using DeCART and CORONA is targeted in this project. The reactor model used for the OECD/NEA MHTGR-350 benchmark problem [7] was selected for the verification of the DeCART/CORONA analysis in this work since the independent numerical benchmark results would be available through the benchmark activity organized by OECD/NEA. Figure 15 shows a layout of the MHTGR-350 core. The main design parameters of the core are provided in Table 8.

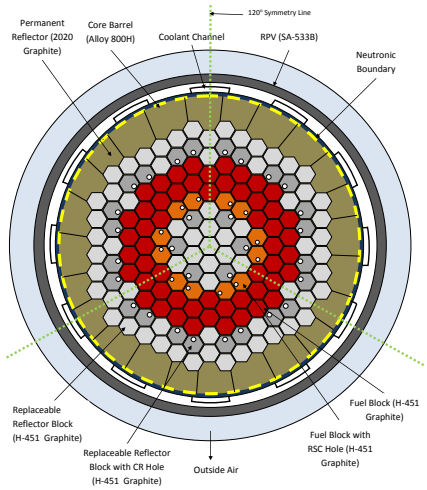

Figure 15. Reactor Core Used for MHTGR-350 Benchmark [7]

In the present period of the project, a preliminary CORONA stand-alone calculation was carried out. The coupled analysis with DeCART is scheduled to be performed in the following year. Only 1/6 section of the MHTGR-350 core was investigated due to symmetry. All fuel and reflector columns were individually modeled. The simulation model includes 9 standard fuel columns, 2 RSC fuel columns, 20 reflector columns, and 5 control reflector columns. The model also contains 1162 coolant channels, 117 bypass gap channels, and 7 control rod channels.

Table 8. Core Design Parameters

Core Parameter	Value	Unit
Thermal Power	350	MW(t)
Number of fuel columns	66	
Coolant inlet temperature	259	^{o}C
Coolant outlet temperature	~687	^{o}C
Total inlet mass flow rate	157.1	kg/s
Coolant outlet pressure	6.39	MPa
Active core height	7.93	m
Number of standard fuel elements	540	10/column
Number of RSC fuel elements	120	
Number of control rods in the Inner reflector	6	
Number of control rods in the Outer reflector	24	
Number of RSC channels in core	12	
Compacts per core (approximate)	2.0358E+06	
Particles per core (approximate)	1.2186E+10	

All the bypass gaps between the columns were fixed to 2mm. The cross-flow gaps were neglected. Under normal operating conditions, the amount of heat removed by the RCCS system is known to be less than ~0.5%. Therefore, the heat loss to the RCCS system was neglected in the preliminary calculation. The power profile specified for Exercise 2 of the MHTGR-350 benchmark was applied. The total numbers of solid and fluid meshes used for the CORONA calculation are 24,486,000 and 112,904, respectively.

Table 9 summarizes the calculated flow distribution by CORONA. The calculated values are well matched with those in the benchmark specification. Figure 16 illustrates the result of the CORONA calculation. It shows the calculated maximum temperature within each column. It clearly shows that the temperatures of the fuel columns are much higher than those of reflector columns. The temperatures of the inner reflector columns are lower than those of adjacent fuel columns due to the convective cooling of the bypass gap flow. The predicted maximum fuel temperature is 1006 ^{o}C, which is sufficiently below the design limit.

Table 9. Calculated Flow Distributions

Regions	Flow Fraction (%)
Main coolant channels	89
Bypass flow through bypass gaps	8
Bypass flow through inner control rod channel	1.2
Bypass flow through inner control rod channel	1.8

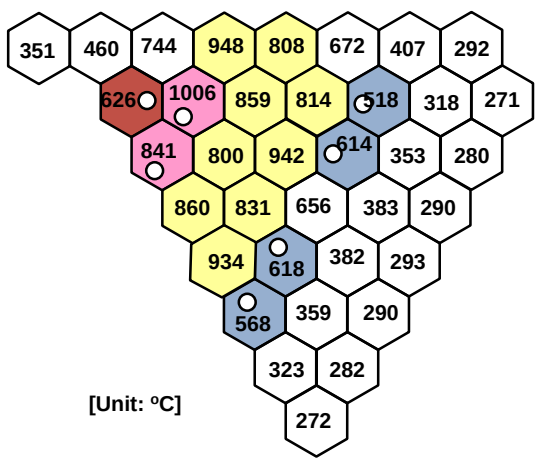

Figure 16. Calculated Maximum Temperature within Each Column

Task 4: Generation and Verification of a Generalized Cross Section Library for Fast and Thermal Reactors (Argonne)

A new task was created from FY13 because the focus of the NEAMS program supporting the I-NERI project was changed from LWR to SFR and accordingly the work scope in the Argonne side had to be altered. This new task is based on the previous Task 2F (generation of a generalized cross section library) which was moved and expanded to include verification activities as well as development of the cross section application programming interface (API).

Task 4A: Generation of a Generalized Cross Section Library (Argonne)

A generalized cross section methodology and library was developed for application to various reactor types including light water reactor (LWR), very high temperature reactor (VHTR), and sodium-cooled fast reactor (SFR). The ultrafine group (2158 groups) cross section library including the resonance integral tables for resonance cross sections was produced by the GeneCS code [8] using the cross section data generated from MC^2-3 [9] and NJOY, as shown in Figure 17. The resonance integral tables were formulated for absorption, nu-fission, and scattering cross sections. The ultrafine group cross section library can be condensed to a broad group library (< 400 groups) using GeneCS for specific use on a target reactor. This is accomplished using a group condensation optimization algorithm which uses a representative neutron spectrum and various homogeneous or pin cell compositions for the reactor type of interest. Note that this is a group condensation process from library to library such that the resulting broad group library can be directly used for any transport code via the cross section application programming interface (API) we have developed during this year. The number of broad groups for the reduced library is determined by a group condensation error criterion. It should be emphasized that this cross section library generation procedure can be used for both the conventional and high-fidelity multi-group cross section generation process.

Since the primary reactor system of interest has been a SFR, we additionally developed a rigorous cross section generation approach using the direct resonance self-shielding method as a high-fidelity cross section generation approach for SFR, in which the MC^2-3 methodology was extended from 1-D geometries to large scale 3-D geometries. This direct resonance self-shielding method can be used when more rigorous and accurate cross sections are required for fast reactor analysis. Unlike the generalized cross section approach, this method is at the moment limited to fast reactor analysis because the development of MC^2-3 was focused exclusively on fast spectrum work and significant research and code modifications are necessary to incorporate thermal reactor analysis. We note that further research and development on the rigorous MC^2-3 approach can improve the generalized cross section library that we developed this year.

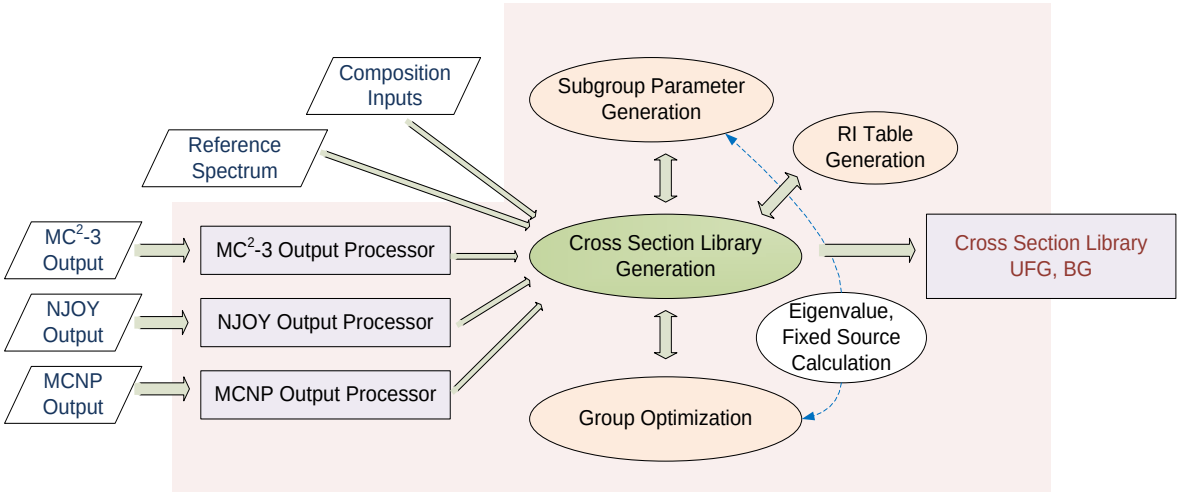

Figure 17. Cross Section Library Generation Using the GeneCS Code

From preliminary investigations on the resonance self-shielding methods, we decided to use the resonance integral (RI) table method which is more simple and robust to determine the resonance table rather than the subgroup method which needs the least square fitting to define subgroup parameters. However, there is no distinct superiority in accuracy between the two methods.

As discussed in the previous section, the resonance cross sections for absorption, nu-fission, and scattering are tabulated as a function of background cross section and temperature for the RI table method. It should be noted that the scattering resonance cross section, which is often missed in the conventional subgroup library, plays an important role in determining the neutron spectrum accurately. Those three resonance integrals are based on the flux approximated with the absorption cross section only. Although the flux approximation is different from the actual flux, it should be fine since the resonance versus background table is determined to reproduce reference solutions.

The observations discussed in the previous section indicated that the resulting multi-group cross sections with more accurate representation of resonance cross sections often showed better agreement on partial cross sections but rather worse agreement on eigenvalue with the reference solutions. This is partly because the group condensation was not accurately conducted for scattering cross sections and matrices.

To minimize errors due to the group condensation procedure, one can increase the number of groups to some extent. Based on the MC^2-3 code development experience for fast reactor systems, the ultrafine groups (UFGs), ~2000 groups, should be a good starting point for generating a base cross section library. We understand that thermal reactor systems do not need that many groups, but fast reactor systems need the UFG cross sections to accurately capture severe spectrum transitions between distinctly different material regions.

Because the UFG structure may contain too many groups for a whole-core transport calculation, it needs to be reduced to a practical number of groups with an appropriate UFG neutron group spectrum. Thus, we propose a way of reducing an UFG library to a broad group (BG) library while minimizing the loss in accuracy. Once a reactor of interest is selected, the UFG transport calculations are first performed with a representative homogeneous composition to determine the UFG neutron spectrum. Next, various possible compositions are used to determine the BG boundaries to best approximate the solutions with the UFG cross section library in terms of partial multi-group cross sections and eigenvalue. This involves an optimization process for group condensation, which will be discussed later in this section. This procedure is similar to the way that the subgroup parameters are determined with many possible fuel compositions and pin cell geometries with various temperature and background cross section conditions.

Once the BG structure is determined, the UFG cross section library is reduced to the BG cross section library using the representative UFG neutron spectrum. This should be differentiated from the conventional cross section library generation practices in that it is not a process of generating a cross section library from a raw nuclide data but a process of reducing an UFG cross section library to a BG library. So, all the resonance tables should be reducible without losing accuracy. This is one of the reasons why we selected the RI table method instead of the subgroup method whose parameters cannot be reduced by a simple group condensation

process. With the cross section table method, the UFG resonance cross sections are simply condensed as

$$\bar{\sigma}_G(\sigma_b, T) = \frac{\sum_{g \in G} \sigma_{\alpha g}(\sigma_b, T)\phi_g^{ref}}{\sum_{g \in G} \phi_g^{ref}}, \tag{12}$$

where α is one of absorption, nu-fission, and scattering, and ϕ_g^{ref} is the representative UFG neutron spectrum for a specific reactor or reactor type. To make the table condensation simple, the same background cross section are used over all resonance UFGs.

An optimized group condensation process is one of the key steps in the proposed cross section library generation methodology. An algorithm for the group structure optimization was devised to search for a BG structure which is insensitive to any change of UFG spectra within a BG. The allowance of sensitivity will be determined by a user as a group optimization criterion. There are two ways to check. One is to check the difference of production and absorption reaction rates, as discussed in Task 1D.

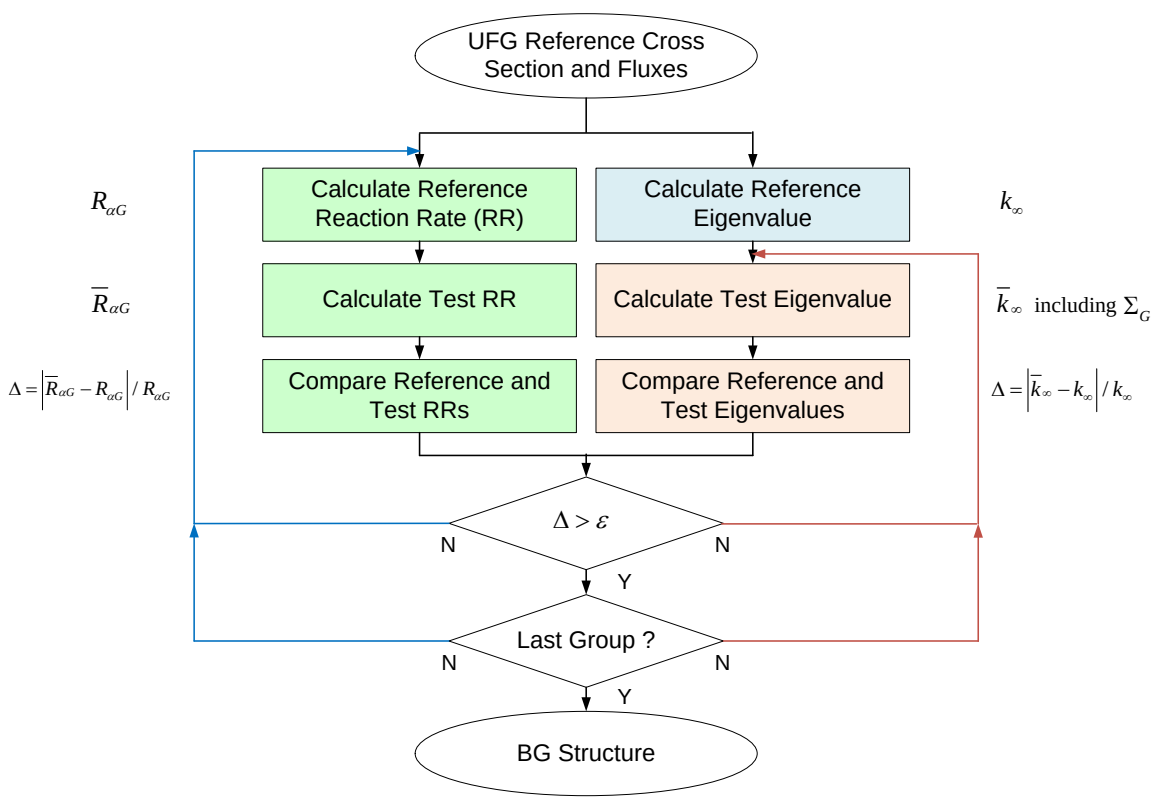

Figure 18. Group Optimization Algorithms from UFG to BG Libraries

This algorithm focuses on the change of two direct components (absorption and production) which determine the eigenvalue with given neutron fluxes, but we found that it overlooks the contribution from the indirect component, scattering cross sections, which affects the neutron spectrum. The other group optimization algorithm is to solve the eigenvalue problem and check

Δk directly whenever adding a UFG to a broad group G. Since a focus of this algorithm is on the change of eigenvalue, this is more tolerant to the change of absorption and fission reaction rates when the change of both reaction rates moves toward the same direction but less tolerant for the other direction. Investigations indicated that the resulting broad groups from this algorithm are better than those from the first one, and therefore we selected the second algorithm for the group condensation in the work here. However, both algorithms could be utilized together to find more rigorous broad group boundaries. Figure 18 depicts the flow of the group optimization algorithms that have been discussed.

Task 4B: Verification of the Generalized Cross Section Library (Argonne)

Various compositions were selected for each reactor type of LWR, VHTR, and SFR to test the generalized cross section library. In order to have a wide range of background cross section for major actinide isotopes such as U-235, U-238, and Pu-239, the isotopic number densities in the compositions were changed. The ultrafine group cross section library was reduced to broad group libraries for specific reactor types using the group optimization process. Details of test results for each reactor type will be discussed in this section.

a) Sodium Fast Reactor

For SFR, seven different compositions were selected as listed in Table 10. Among them, Cases 1, 3, and 7 came from the MC^2-3 core benchmark problems: Cases 1 and 3 are composed of 21 and 16 wt% Pu contents, respectively, and structural material, while Case 7 is a typical blanket composition. For simplicity, only the isotope with the largest abundance ratio from elements, such as Fe, Cr, Ni, Mo, and Zr, was included in the compositions. Case 2 was fetched from the two-region benchmark problems of MC^2-3 which were used to check the resonance interaction between U-238 and Fe-56. In Cases 4, 5, and 6, the number densities of U-238 and Pu-239 only were changed with maintaining the other isotopes' number densities (Fe-56, Na-23, and O-16) the same: the plutonium contents of the three compositions are 16, 38, and 13 wt%, respectively. The neutron spectra for the compositions are shown in Figure 19. As seen in the figure, all cases show a typical neutron spectrum of fast reactors. Among them, Case 2 (red) shows an extreme change of neutron spectrum over energy due to a relatively large amount of Fe-56 included in the composition.

Table 10. Isotopes and Number Densities of Sodium Fast Reactor Compositions

Case	1		2		3		4		5		6		7	
Isotope &	U-235	1.11E-05	U-235	7.00E-04	U-235	1.44E-05	U-238	5.00E-03	U-238	7.00E-03	U-238	6.00E-03	U-235	1.59E-05
Number	U-238	5.49E-03	U-238	5.00E-03	U-236	9.20E-07	Pu-239	3.00E-03	Pu-239	1.00E-03	Pu-239	2.00E-03	U-238	7.53E-03
Density	Pu-239	9.11E-04	Pu-239	9.11E-04	U-238	9.05E-03	O-16	2.00E-02	O-16	1.60E-02	O-16	1.60E-02	Cr-50	1.67E-04
	Pu-240	3.52E-04	Fe-56	4.00E-01	Pu-239	1.57E-03	Fe-56	8.00E-03	Fe-56	2.00E-02	Fe-56	2.00E-02	Fe-56	1.26E-02
	Pu-241	1.03E-04			Pu-240	1.67E-04	Na-23	1.60E-02	Na-23	8.00E-03	Na-23	8.00E-03	Ni-58	1.84E-03
	Pu-242	5.79E-05			Pu-241	1.10E-05							Mo-92	4.54E-05
	Cr-50	3.22E-03			Pu-242	7.85E-07							Na-23	9.44E-03
	Fe-56	1.26E-02			Cr-50	1.05E-04							Mn-55	3.64E-04
	Ni-58	1.84E-03			Fe-56	1.49E-02							O-16	1.51E-02
	Mo-92	4.54E-05			Ni-58	6.80E-05								
	Na-23	9.44E-03			Mo-92	8.17E-05								
	O-16	1.37E-02			Na-23	7.15E-03								
					Mn-55	1.07E-04								
					Zr-90	1.68E-03								

Reference solutions were generated using MCNP5 and MC^2-3. As shown in Table 11 the maximum difference in eigenvalue between the two codes is 144 pcm. The eigenvalue solutions from the RI table method with the 2158 group library (using the Bondarenko iteration for resonance self-shielding) agreed with MCNP5 solutions within 196 pcm. This accuracy in eigenvalue is much better than expected, but we noticed that the differences in the detailed UFG cross sections are not negligible. This implies that the RI table method with the Bondarenko iteration resulted in good eigenvalue solutions due to some cancellation of errors. This is similar to the observation that was made when testing the subgroup method for SFR compositions, with which the errors in the detailed broad group cross sections became reduced with a smaller number of energy groups.

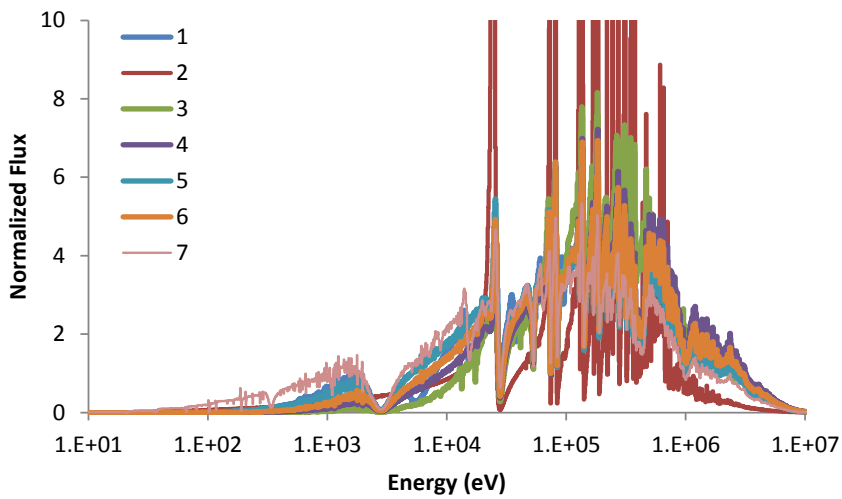

Figure 19. Neutron Spectra of Sodium Fast Reactor Compositions

The group condensation was performed using Cases 1, 2, and 4 as variable compositions and Case 5 as the representative UFG neutron spectrum composition. The criterion of Δk for each broad group was set to 5, 20, and 50 pcm in the group optimization process in GeneCS. The resulting broad group structures are 383, 219, and 142 groups for a Δk criterion of 5, 20, and 50 pcm, respectively. The eigenvalues from the broad group libraries agreed with the MCNP5 solutions within 225, 230, and 327 pcm Δk, as shown in Table 11. When using the existing group structures: the ANL 230 group structure, the DeCART 190 group structure, and the SCALE (ORNL) 238 group structure [10], most cases showed reasonably small differences in eigenvalue from the MCNP5 solutions but very large errors were observed in Case 2 (the most difficult case in terms of neutron spectrum transition) for all exiting group structures and Case 3 for the ORNL group structure. The differences came mainly from the overestimation of Fe-56 scattering cross sections over 100 keV, which led to the softer neutron spectrum resulting in the large underestimation of eigenvalue.

Figure 20 compares the resulting broad group structures, from which the lethargy plots are shown from the smallest (top) to largest (bottom) number of groups. As seen in the figure, many groups were assigned to the energy ranges for actinide (tens – hundreds eV) and intermediate-weight (hundreds keV) isotope resonances. Compared were the percent differences of total cross sections of U-238 between MC^2-3 and the RI table method, which includes the results from 2158, 383, 219, and 142 group libraries. Note that while all the BG cross sections from MC^2-3 are

condensed from the 2158-group cross sections, those from the RI table method are the solutions from each BG transport calculation. Because of no overlapping of resolved resonances between different isotopes above 20 keV, the cross sections from the RI table method are in good agreement with those from MC^2-3. However, large differences in the UFG cross sections between the two codes are observed below 2 keV for U-238 and Pu-238. The magnitudes of the differences become reduced significantly with smaller number of energy groups, which is apparently due to the cancellation effect.

Table 11. Eigenvalue Comparison for Sodium Fast Reactor Compositions

Case	MCNP5	MC^2-3	UFG(Δk)	BG (Δk)			Existing BG (Δk)		
			2158G	383	219	142	ANL230	ORNL238	DeC 190
1	1.35803	118	143	161	155	116	307	93	337
2	1.09527	-71	-169	-3	230	327	-1771	-6064	-3876
3	1.63860	-8	-196	-225	-230	-278	-177	-806	-291
4	2.06932	28	-101	-95	-83	-113	-81	-278	-180
5	1.24105	144	184	214	208	278	166	204	215
6	1.75072	64	-8	17	41	60	36	-50	-1
7	0.18888	54	73	88	32	-12	18	19	59

∗ Standard deviation of MCNP5 solutions ≤ 30 pcm
∗ The UFG and BG columns show differences in eigenvalue, pcm, from MCNP5

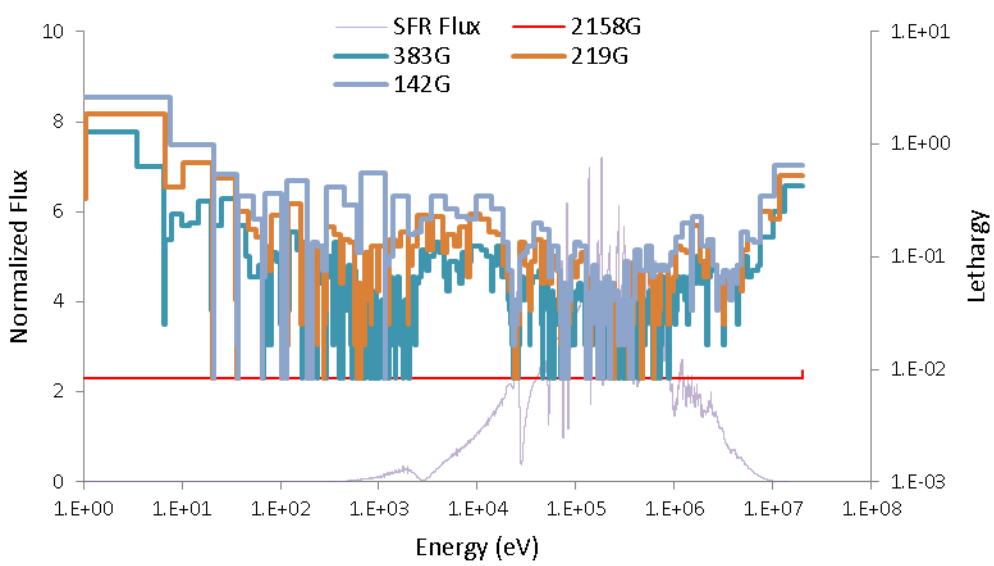

Figure 20. Lethargy Intervals of the Broad Group Structures for Sodium Fast Reactor

b) Light Water Reactor

For LWR, six different compositions were selected. The composition of Case 1 is a typical LWR fuel composition. The other cases were created by modifying the Case 1 number densities of U-235 and U-238. Consequently, U-235 enrichments were increased for Cases 2 (24 wt%), 3 (75 wt%), and 5 (96 wt%) and decreased for Cases 4 and 6 (almost natural uranium). These cases were created to provide different background cross sections to two major actinides, U-235 and U-238, in LWR, even though some of the compositions are unrealistic.

The compositions for the six test cases are listed in Table 12. Figure 21 depicts neutron spectra for those six cases. Cases 4 and 6, which have almost natural uranium, show higher thermal neutron fluxes while the other cases with U-235 enrichments of 3 to 96 wt% produces relatively higher fast neutron fluxes, as expected. The neutron flux wiggles are shown in the resonance energy range from a few eV to a few hundreds keV.

Table 12. Isotopes and Number Densities of Light Water Reactor Compositions

Case	1		2		3		4		5		6	
Isotope &	U-234	2.03E-06	U-234	2.03E-06	U-234	2.03E-06	U-234	2.03E-06	U-234	2.03E-06	U-234	2.03E-06
Number	U-235	2.38E-04	U-235	2.38E-04	U-235	2.38E-04	U-235	2.38E-05	U-235	2.38E-04	U-235	2.38E-06
Density	U-236	1.10E-06	U-236	1.10E-06	U-236	1.10E-06	U-236	1.10E-06	U-236	1.10E-06	U-236	1.10E-06
	U-238	7.36E-03	U-238	7.36E-04	U-238	7.36E-05	U-238	7.36E-03	U-238	7.36E-06	U-238	7.36E-03
	O-16	2.89E-02	O-16	2.89E-02	O-16	2.89E-02	O-16	2.89E-02	O-16	2.89E-02	O-16	2.89E-02
	Zr-90	4.28E-03	Zr-90	4.28E-03	Zr-90	4.28E-03	Zr-90	4.28E-03	Zr-90	4.28E-03	Zr-90	4.28E-03
	H-1	2.75E-02	H-1	2.75E-02	H-1	2.75E-02	H-1	2.75E-02	H-1	2.75E-02	H-1	2.75E-02

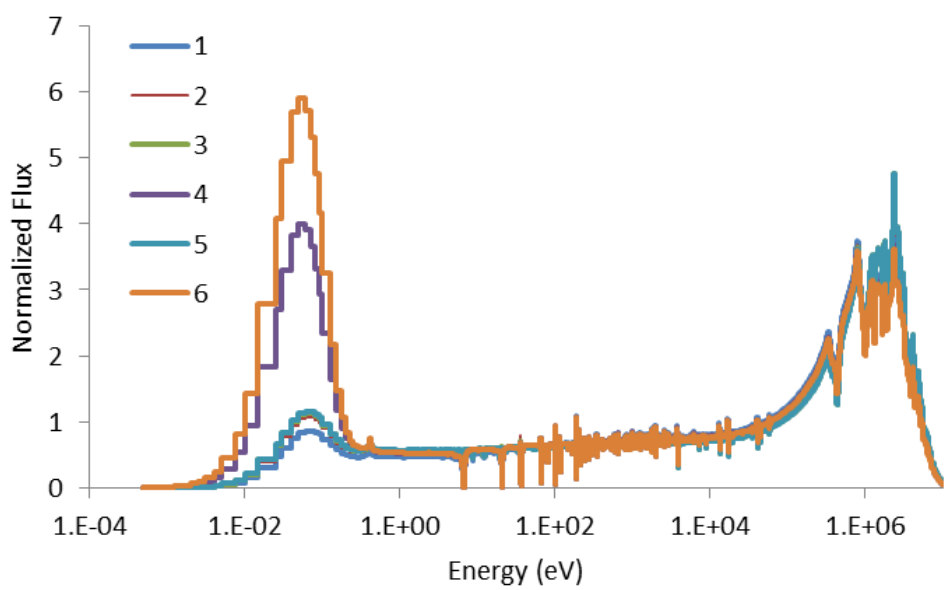

Figure 21. Neutron Spectra of Light Water Reactor Compositions

The group condensation was performed using Cases 1, 2, and 4 as variable compositions and Case 1 as the representative UFG neutron spectrum composition. In the same manner as SFR, the

criterion of Δk for each broad group was set to 5, 20, and 50 pcm in the group optimization process of GeneCS. The resulting broad groups were 204, 120, and 78 groups for a Δk criterion of 5, 20, and 50 pcm, respectively. The resulting numbers of broad groups with the same stopping criteria for determining group boundaries are smaller than those for SFR. This is because coarser groups were determined in the high energy range which are more important to SFR but less important to LWR.

Table 13. Eigenvalue Comparison for Light Water Reactor Compositions

Case	MCNP5	UFG(Δk)	BG (Δk)			Existing BG (Δk)	
		2158G	204	120	78	ORNL238	DeC 190
1	1.28101	-85	-75	-90	-62	-118	-69
2	1.70407	-91	-186	20	183	4982	5515
3	1.83689	11	-88	28	109	2670	2850
4	0.58602	198	160	144	61	179	159
5	1.87309	108	25	109	140	565	657
6	0.15768	127	165	144	131	152	145

∗ Standard deviation of MCNP5 solutions ≤ 30 pcm
∗ The UFG and BG columns show differences in eigenvalue, pcm, from MCNP5

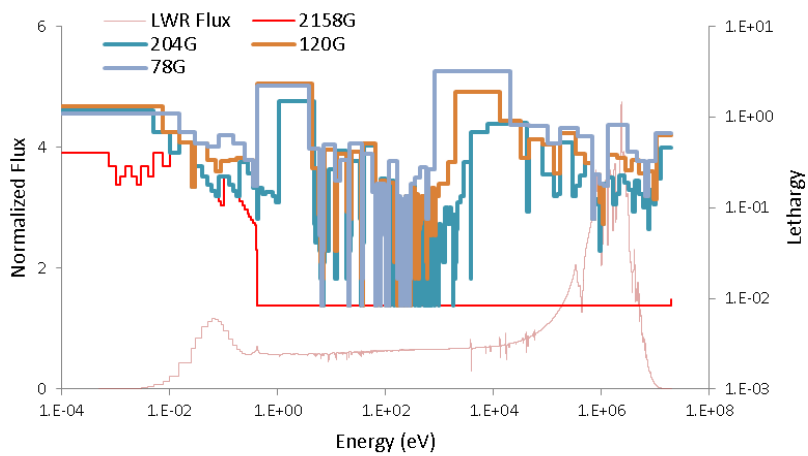

Figure 22. Lethargy Intervals of the Broad Group Structures for Light Water Reactor

Reference solutions were generated using MCNP5. As shown in Table 13, the eigenvalue solutions from the RI table method with the 2158 group library (using the Bondarenko iteration for resonance self-shielding) agreed with MCNP5 solutions within 198 pcm. The eigenvalues from the broad group libraries with 204, 120, and 78 groups were off from the MCNP5 solutions by maximum 186, 144, and 183 pcm Δk, respectively. When using the existing group structures: the DeCART 190 group structure and the SCALE (ORNL) 238 group structure, Cases 1, 4, and 6 showed reasonably small differences in eigenvalue from the MCNP5 solutions, while very large errors were observed in Cases 2, 3, and 5 for all exiting group structures, in which the U-238 number densities are relatively small and thus the U-235 enrichment becomes high. The

differences came mainly from the large underestimation of U-238 absorption cross sections in the energy range between 6.7 and 100 eV which resulted in the large overestimation of eigenvalue. The underestimation of eigenvalue in Case 3 is smaller than in Case 2 since the number density of U-238 in Case 3 is smaller by an order of magnitude than in Case 2.

Similarly to the SFR cases, Figure 22 compares the resulting broad group structures, from which the lethargy plots are shown from the smallest (top) to largest (bottom) number of groups. Many groups were assigned to the energy ranges for actinides (tens – hundreds eV), as shown in the figure.

c) Very High Temperature Reactor

For VHTR, seven different compositions were selected as listed in Table 14. The composition of Case 1 (14 wt% U-235) is a typical VHTR fuel composition. The other cases were created by modifying the number densities of U-235, U-238, or other isotopes of the Case 1 composition. These changes increased U-235 enrichments up to 89 wt% for Cases 6 and 7. The carbon number density was increased to mimic the neutron spectrum for a fuel block or a whole core where a large thermal spectrum peak appears, as shown in Figure 23. These cases were created to provide various background cross sections to two major actinides, U-235 and U-238, in VHTR.

As shown in Figure 23, the neutron spectra have relatively large neutron fluxes in the intermediate energy range, compared to the LWR spectrum. Therefore, the more number of energy groups in VHTR than in LWR are expected in the epi-thermal energy range.

The group condensation was performed using Cases 1, 2, and 5 as variable compositions and Case 6 as the representative UFG neutron spectrum composition. In the same manner as other reactor types, the criterion of Δk for each broad group was set to 5, 20, and 50 pcm in the group optimization process of GeneCS. The resulting broad groups were 198, 113, and 76 groups for a Δk criterion of 5, 20, and 50 pcm, respectively. Similar to LWR, the resulting numbers of broad groups with the same stopping criteria for determining group boundaries are smaller than those for SFR. It is interesting to note that the number of broad groups for VHTR is similar to those for LWR, even though the allocation of group boundaries are different each other.

Reference solutions were generated using MCNP5. As shown in Table 15, the eigenvalue solutions from the RI table method with the 2158 group library (using the Bondarenko iteration for resonance self-shielding) agreed with MCNP5 solutions within 174 pcm. The eigenvalues from the broad group libraries with 198, 113, and 76 groups were off from the MCNP5 solutions by maximum 195, 244, and 317 pcm Δk, respectively. Note that all the largest errors came from Case 7 which is a kind of extreme case with very large amount of carbon. When using the existing group structures: the DeCART 190 group structure and the SCALE (ORNL) 238 group structure, Cases 1 and 7 showed reasonably small differences in eigenvalue from the MCNP5 solutions but very large errors were observed in most cases (Cases 2 through 6) for all exiting group structures. For the existing group structures, in fact, we switched the representative spectrum from Case 6 to Case 1 because Cases 1 to 4 resulted in more than 20% error in eigenvalue with the representative spectrum of Case 6. The results indicate that the existing group structures are very sensitive to the choice of the representative spectrum, whereas the broad group structures generated by GeneCS show no noticeable changes in eigenvalue no

matter which representative spectrum was used. In the existing group structures, the eigenvalue differences are caused by over- and under-estimation of U-238 absorption cross sections in the energy range between 6.7 and 200 eV, similarly to the LWR cases. Figure 24 compares the resulting broad group structures, from which the lethargy plots are shown from the smallest (top) to largest (bottom) number of groups.

Table 14. Isotopes and Number Densities of High Temperature Reactor Compositions

Case	1		2		4		4		5		6		7	
Isotope &	U-235	1.06E-04	U-235	1.06E-04	U-235	1.06E-04	U-235	1.06E-04	U-235	1.06E-04	U-235	1.06E-04	U-235	1.06E-04
Number	U-238	6.45E-04	U-238	6.45E-04	U-238	1.29E-03	U-238	3.23E-04	U-238	6.45E-05	U-238	1.29E-05	U-238	1.29E-05
Density	O-16	1.13E-03	O-16	1.13E-03	O-16	1.13E-03	O-16	1.13E-03	O-16	1.13E-03	O-16	1.13E-02	O-16	2.26E-02
	C-12	6.06E-02	C-12	1.31E-01	C-12	6.06E-02	C-12	6.06E-02	C-12	6.06E-02	C-12	6.06E-01	C-12	1.21E+00
	Si-28	2.52E-03	Si-28	2.52E-03	Si-28	2.52E-03	Si-28	2.52E-03	Si-28	2.52E-03	Si-28	2.52E-02	Si-28	5.03E-02

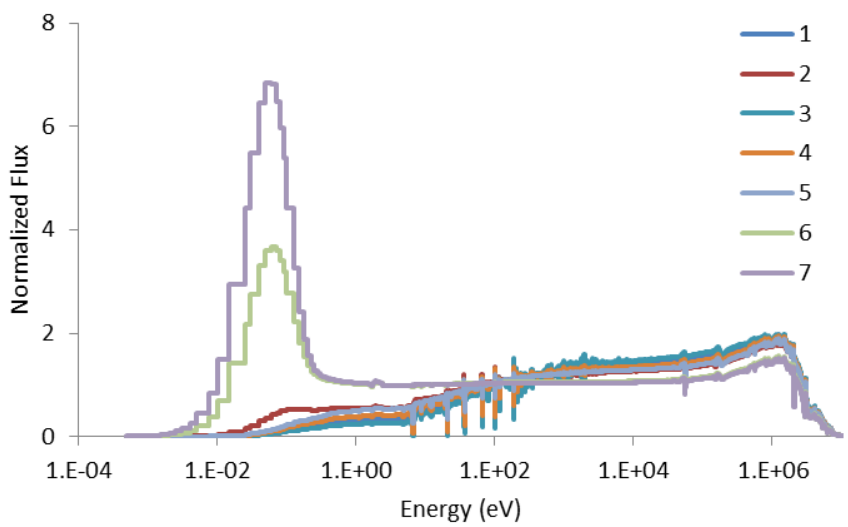

Figure 23. Neutron Spectra of High Temperature Reactor Compositions

Table 15. Eigenvalue Comparison for High Temperature Reactor Compositions

Case	MCNP5	UFG(Δk)	BG (Δk)			Existing BG (Δk)	
		2158G	198	113	76	ORNL238	DeC 190
1	1.06282	111	57	109	168	106	144
2	1.21039	79	52	131	231	6670	7584
3	0.86047	102	-64	101	-28	-4545	-5704
4	1.23983	72	51	88	123	5018	5755
5	1.53891	-33	-106	-143	-200	8660	9402
6	1.84899	-99	-101	-72	-79	787	863
7	1.73383	-174	-195	-244	-317	250	272

∗ Standard deviation of MCNP5 solutions ≤ 30 pcm

∗ The UFG and BG columns show differences in eigenvalue, pcm, from MCNP5

As aforementioned, the GeneCS code produces the cross section library in a DeCART library format. Using the selected cases for LWR, VHTR, and SFR, the code generated the BG cross section libraries as well as the UFG cross section libraries for each reactor type. We updated DeCART to use the RI table method in terms of absorption, nu-fission, and scattering resonance cross sections. The UFG or BG cross section library can be directly read by DeCART. All results produced by the GeneCS code have been reproduced in DeCART.

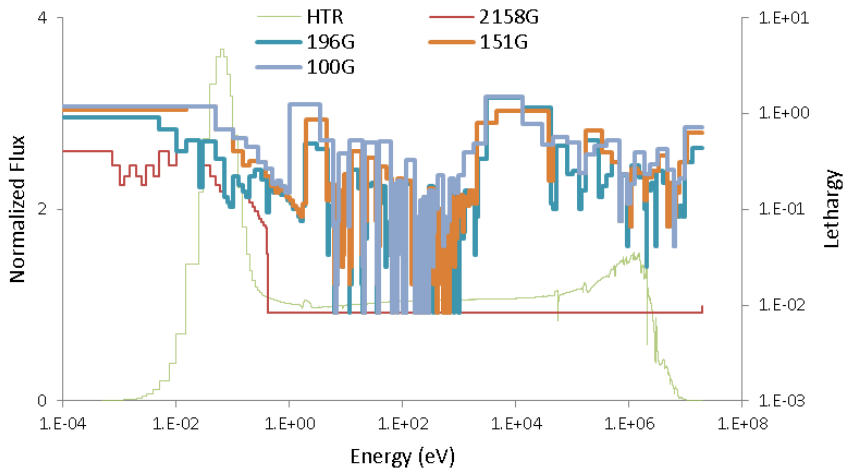

Figure 24. Lethargies of the Broad Group Structures for High Temperature Reactor

Task 4C : Development of a Cross Section Application Programming Interface(API) (Argonne)

The cross section application programming interface (API) was developed to make it easier to implement the cross section generation tool into any transport code. First, the subgroup method was selected as a cross section generation method. The subgroup API is divided into two parts: the subgroup-independent and -dependent ones. The subgroup-independent part is composed of setting-up, defining, reading & storing, and cleaning-up data, while the subgroup-dependent part contains the routines calling the fixed-source solver, handling the subgroup parameters, and conducting the Bondarenko iteration. When other cross section methods are used, only the method-dependent part needs to be updated.

The subgroup API reads isotopic data from the cross section library and the cross section region mapping information as well. Once all subgroup cross section data are specified and read from and written to necessary data files, the subgroup API generates the region-wise escape cross sections using the one-group (i.e., group-independent) whole-core fixed-source solver provided by the transport code. Therefore, one may expect to change a transport code to separate out a fixed-source transport solver in the manner as directed by the API. This would not be difficult since most transport codes should have an independent subroutine or module to solve for $AX = B$. To calculate the escape cross sections, the API sets up relevant cross sections and sources for the fixed-source solver. A do-loop is necessary to cover all energy groups and an iteration algorithm may be needed to converge cross sections and fixed sources depending upon

the cross section method of choice. Figure 25 shows a developmental scheme on how the transport solver and the subgroup API interact. The subgroup API has been integrated into PROTEUS. Preliminary test results with pin cell and small lattice problems indicated its successful implementation to the transport code.

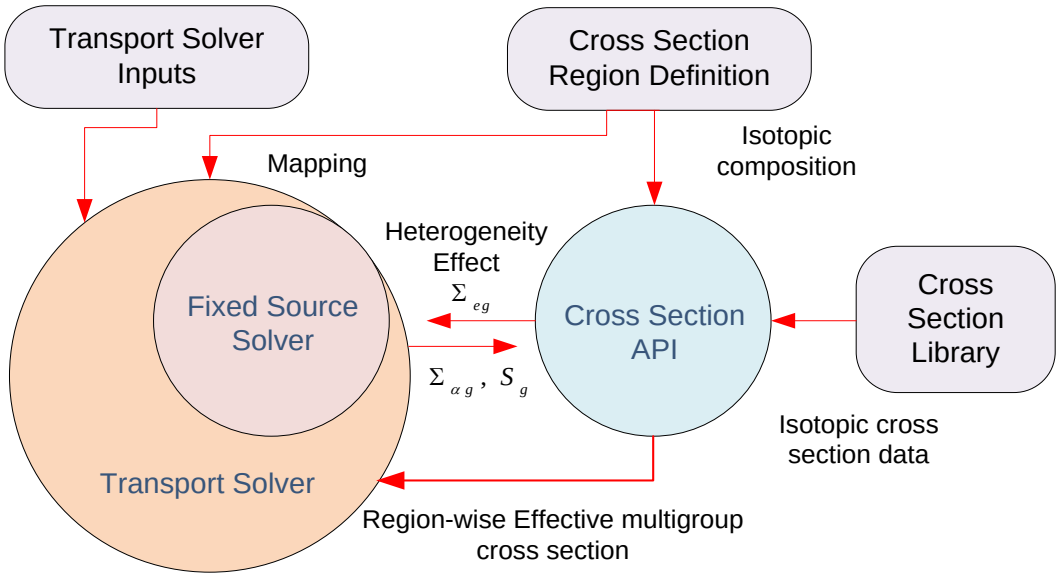

Figure 25. Interaction between the Cross Section API and the Neutron Transport Solver

References

1. N. NOJIRI, et al., "Benchmark Problems' Data for the HTTR's Start-up Core Physics Experiments," JAERI-memo 10-005, January, 1998.
2. "Data for re-calculation of HTTR-FC," An addendum to JAERI-memo 10-005.
3. K. S. Kim, "Development of a physics analysis procedure for the prismatic very high temperature gas-cooled reactors," *Ann. Nucl. Eng*. **34**, 849-860, 2007.
4. H. C. Lee, et al., "Reduction of Azimuthal Angle Discretization Error in Method of Characteristics," Transactions of the American Nuclear Society, Vol. 108, Atlanta, Georgia, June 16–20, 2013.
5. S. G. Hong and K. S. Kim, "Iterative Resonance Self-Shielding Methods Using Resonance Integral Table in Heterogeneous Transport Lattice Calculation," *Ann. Nucl. Eng*. **38**, 32-43, 2011.
6. S. Y. Park, et al., "KARMA 1.2 User's Manual," KAERI/UM-19/2012, 2012.
7. Prismatic Coupled Neutronics/Thermal Fliuds Transient Benchmark of the MHTGR-350MW Core Design – Benchmark Definition, Draft Date : 07/16/2013, (https://oecd-mhtgr-350.inl.gov).
8. C. H. Lee, A. Marin-Lafleche, and M. A. Smith, "Development of Cross Section Library and Application Programming Interface (API)," ANL/NE-13/15, September, 2013.
9. C. H. Lee and W. S. Yang, "MC^2-3: Multigroup Cross Section Generation Code for Fast Reactor Analysis," ANL/NE-11-41, January, 2012.

10. SCALE: A Comprehensive Modeling and Simulation Suite for Nuclear Safety Analysis and Design, ORNL/TM-2005/39, Version 6.1, Oak Ridge National Laboratory, Oak Ridge, Tennessee, June 2011.

Project Milestone/Deliverable Summary:

Milestone/Deliverable Description	Planned Completion Date	Actual Completion Date
First Year Annual Report	09/30/2012	09/30/2012
Second Year Annual Report	10/31/2013	10/31/2013
Final Report		

Task #	Months											
	3	6	9	12	15	18	21	24	27	30	33	36
0.0												
0.1												
1.0												
1A	K											
1B		K										
1C								K				
1D			K									
1E	K											
2.0												
2A	A											
2B	A											
3.0												
3A								K				
4.0												
4A					A							
4B					A							
4C					A							

* A : Argonne, K: KAERI

Nuclear Engineering Division
Argonne National Laboratory
9700 South Cass Avenue, Bldg. 208
Argonne, IL 60439

www.anl.gov

Argonne National Laboratory is a U.S. Department of Energy
laboratory managed by UChicago Argonne, LLC